Editors' Suggestion Featured in Physics

Antiprotons and Elementary Particles over a Solar Cycle: Results from the Alpha Magnetic Spectrometer

M. Aguilar,[29] G. Ambrosi,[35] H. Anderson,[10] L. Arruda,[27] N. Attig,[24] C. Bagwell,[10] F. Barao,[27] M. Barbanera,[35] L. Barrin,[14] A. Bartoloni,[39] R. Battiston,[46,47] A. Bayyari,[20] N. Belyaev,[10] B. Bertucci,[35,36] V. Bindi,[20] K. Bollweg,[21] J. Bolster,[10] M. Borchiellini,[17] B. Borgia,[39,40] M. J. Boschini,[31] M. Bourquin,[15] C. Brugnoni,[35,36] J. Burger,[10] W. J. Burger,[46] X. D. Cai,[10] M. Capell,[10] J. Casaus,[29] G. Castellini,[13] F. Cervelli,[37] Y. H. Chang,[44] G. M. Chen,[6,7] G. R. Chen,[23] H. Chen,[19] H. S. Chen,[6,7] Y. Chen,[23] L. Cheng,[23] H. Y. Chou,[44] S. Chouridou,[1] V. Choutko,[10] C. H. Chung,[1] C. Clark,[10,21] G. Coignet,[3] C. Consolandi,[20] A. Contin,[8,9] C. Corti,[20] Z. Cui,[22,23] K. Dadzie,[10] F. D'Angelo,[9,8] A. Dass,[46,47] C. Delgado,[29] S. Della Torre,[31] M. B. Demirköz,[2] L. Derome,[16] S. Di Falco,[37] V. Di Felice,[41] C. Díaz,[29] F. Dimiccoli,[46,47] P. von Doetinchem,[20] F. Dong,[33] M. Duranti,[35] A. Egorov,[10] A. Eline,[10] F. Faldi,[35,36] D. Fehr,[1] J. Feng,[18] E. Fiandrini,[35,36] P. Fisher,[10] V. Formato,[41] R. J. García-López,[26] C. Gargiulo,[14] H. Gast,[1] M. Gervasi,[31,32] F. Giovacchini,[29] D. M. Gómez-Coral,[30] J. Gong,[33] D. Grandi,[31,32] M. Graziani,[35,36] S. Haino,[44] K. C. Han,[28] R. K. Hashmani,[2] Z. H. He,[18] B. Heber,[25] F. Hernández-Nicolás,[29] T. H. Hsieh,[10] J. Y. Hu,[35] B. W. Huang,[19] M. Ionica,[35] M. Incagli,[37] Yi Jia,[10] H. Jinchi,[28] G. Karagöz,[2] Th. Kirn,[1] A. P. Klipfel,[10] O. Kounina,[10] A. Kounine,[10] V. Koutsenko,[10] D. Krasnopevtsev,[10] A. Kuhlman,[20] A. Kulemzin,[10] G. La Vacca,[31,32] E. Laudi,[14] G. Laurenti,[8] G. LaVecchia,[10] I. Lazzizzera,[46,47] H. T. Lee,[43] S. C. Lee,[44] H. L. Li,[23] J. H. Li,[22] J. Q. Li,[33] M. Li,[15] M. Li,[22] Q. Li,[33] Q. Li,[22] Q. Y. Li,[23] S. Li,[1] S. L. Li,[6] Z. H. Li,[6,7] M. J. Liang,[6,7] P. Liao,[22] C. H. Lin,[44] T. Lippert,[24] J. H. Liu,[5] P. C. Liu,[23] S. Q. Lu,[6,44] Y. S. Lu,[6,†] J. Z. Luo,[33] Q. Luo,[18] S. D. Luo,[19] Xi Luo,[23] C. Mañá,[29] J. Marín,[29] J. Marquardt,[25] G. Martínez,[29] N. Masi,[8] D. Maurin,[16] T. Medvedeva,[10] A. Menchaca-Rocha,[30] Q. Meng,[33] V. V. Mikhailov,[23] M. Molero,[26] P. Mott,[10,21] L. Mussolin,[35,36] Y. Najafi Jozani,[1] R. Nicolaidis,[47,46] N. Nikonov,[20] F. Nozzoli,[46] J. Ocampo-Peleteiro,[29] A. Oliva,[8] M. Orcinha,[35,36] F. Palmonari,[8,9] M. Paniccia,[15] A. Pashnin,[10] M. Pauluzzi,[35,36] D. Pelosi,[35,36] S. Pensotti,[31,32] P. Pietzcker,[25] V. Plyaskin,[10] S. Poluianov,[34] D. Pridöhl,[1] Z. Y. Qu,[23] L. Quadrani,[8,9] P. G. Rancoita,[31] D. Rapin,[15] A. Reina Conde,[8] E. Robyn,[8] I. Rodríguez-García,[29] L. Romaneehsen,[25] F. Rossi,[47,46] A. Rozhkov,[10] D. Rozza,[31,32] R. Sagdeev,[11] S. Schael,[1] A. Schultz von Dratzig,[1] G. Schwering,[1] E. S. Seo,[12] B. S. Shan,[4] A. Shukla,[20] T. Siedenburg,[1] G. Silvestre,[35] J. W. Song,[22] X. J. Song,[23] R. Sonnabend,[1] L. Strigari,[39,*] T. Su,[23] Q. Sun,[22] Z. T. Sun,[6] L. Tabarroni,[41] M. Tacconi,[31,32] Z. C. Tang,[6] J. Tian,[41] Y. Tian,[19] Samuel C. C. Ting,[10,14] S. M. Ting,[10] N. Tomassetti,[35,36] J. Torsti,[48] A. Ubaldi,[35,36] T. Urban,[10,21] I. Usoskin,[34] V. Vagelli,[38,35] R. Vainio,[48] P. Väisänen,[35,36] M. Valencia-Otero,[45] E. Valente,[39,40] E. Valtonen,[48] M. Vázquez Acosta,[26] M. Vecchi,[17] M. Velasco,[29] C. X. Wang,[22] J. C. Wang,[6] L. Wang,[5] L. Q. Wang,[22] N. H. Wang,[22] Q. L. Wang,[5] S. Wang,[20] X. Wang,[10] Z. M. Wang,[23] J. Wei,[15,23] Z. L. Weng,[10] H. Wu,[33] Y. Wu,[23] Z. B. Wu,[22] J. N. Xiao,[19] R. Q. Xiong,[33] X. Z. Xiong,[19] W. Xu,[22,23] Q. Yan,[10] H. T. Yang,[6,7] Y. Yang,[42] H. Yi,[33] Y. H. You,[6,7] Y. M. Yu,[10] Z. Q. Yu,[6] C. Zhang,[6] F. Z. Zhang,[6] J. Zhang,[22] J. H. Zhang,[33] Z. Zhang,[10] P. W. Zhao,[18] C. Zheng,[23] Z. M. Zheng,[4] H. L. Zhuang,[6] V. Zhukov,[1] A. Zichichi,[8,9] M. Zuberi,[10] and P. Zuccon[46,47]

(AMS Collaboration)

[1]*I. Physics Institute and JARA-FAME, RWTH Aachen University, 52056 Aachen, Germany*
[2]*Department of Physics, Middle East Technical University (METU), 06800 Ankara, Türkiye*
[3]*Université Grenoble Alpes, Université Savoie Mont Blanc, CNRS, LAPP-IN2P3, 74000 Annecy, France*
[4]*Beihang University (BUAA), Beijing, 100191, China*
[5]*Institute of Electrical Engineering (IEE), Chinese Academy of Sciences, Beijing, 100190, China*
[6]*Institute of High Energy Physics (IHEP), Chinese Academy of Sciences, Beijing, 100049, China*
[7]*University of Chinese Academy of Sciences (UCAS), Beijing, 100049, China*
[8]*INFN Sezione di Bologna, 40126 Bologna, Italy*
[9]*Università di Bologna, 40126 Bologna, Italy*
[10]*Massachusetts Institute of Technology (MIT), Cambridge, Massachusetts 02139, USA*
[11]*East-West Center for Space Science, University of Maryland, College Park, Maryland 20742, USA*
[12]*IPST, University of Maryland, College Park, Maryland 20742, USA*
[13]*CNR-IROE, 50125 Firenze, Italy*
[14]*European Organization for Nuclear Research (CERN), 1211 Geneva 23, Switzerland*
[15]*DPNC, Université de Genève, 1211 Genève 4, Switzerland*
[16]*Université Grenoble Alpes, CNRS, Grenoble INP, LPSC-IN2P3, 38000 Grenoble, France*

[17]*Kapteyn Astronomical Institute, University of Groningen, P.O. Box 800, 9700 AV Groningen, Netherlands*
[18]*Sun Yat-Sen University (SYSU), Guangzhou, 510275, China*
[19]*Zhejiang University (ZJU), Hangzhou 310058, China*
[20]*Physics and Astronomy Department, University of Hawaii, Honolulu, Hawaii 96822, USA*
[21]*National Aeronautics and Space Administration Johnson Space Center (JSC), Houston, Texas 77058, USA*
[22]*Shandong University (SDU), Jinan, Shandong, 250100, China*
[23]*Shandong Institute of Advanced Technology (SDIAT), Jinan, Shandong, 250100, China*
[24]*Jülich Supercomputing Centre and JARA-FAME, Research Centre Jülich, 52425 Jülich, Germany*
[25]*Institut für Experimentelle und Angewandte Physik, Christian-Albrechts-Universität zu Kiel, 24118 Kiel, Germany*
[26]*Instituto de Astrofísica de Canarias (IAC), 38205 La Laguna and Departamento de Astrofísica, Universidad de La Laguna, 38206 La Laguna, Tenerife, Spain*
[27]*Laboratório de Instrumentação e Física Experimental de Partículas (LIP), 1649-003 Lisboa, Portugal*
[28]*National Chung-Shan Institute of Science and Technology (NCSIST), Longtan, Tao Yuan, 32546, Taiwan*
[29]*Centro de Investigaciones Energéticas, Medioambientales y Tecnológicas (CIEMAT), 28040 Madrid, Spain*
[30]*Instituto de Física, Universidad Nacional Autónoma de México (UNAM), Ciudad de México, 01000 Mexico*
[31]*INFN Sezione di Milano-Bicocca, 20126 Milano, Italy*
[32]*Università di Milano-Bicocca, 20126 Milano, Italy*
[33]*Southeast University (SEU), Nanjing, 210096, China*
[34]*Sodankylä Geophysical Observatory and Space Physics and Astronomy Research Unit, University of Oulu, 90014 Oulu, Finland*
[35]*INFN Sezione di Perugia, 06100 Perugia, Italy*
[36]*Università di Perugia, 06100 Perugia, Italy*
[37]*INFN Sezione di Pisa, 56100 Pisa, Italy*
[38]*Agenzia Spaziale Italiana (ASI), 00133 Roma, Italy*
[39]*INFN Sezione di Roma 1, 00185 Roma, Italy*
[40]*Università di Roma La Sapienza, 00185 Roma, Italy*
[41]*INFN Sezione di Roma Tor Vergata, 00133 Roma, Italy*
[42]*National Cheng Kung University, Tainan, 70101, Taiwan*
[43]*Academia Sinica Grid Center (ASGC), Nankang, Taipei, 11529, Taiwan*
[44]*Institute of Physics, Academia Sinica, Nankang, Taipei, 11529, Taiwan*
[45]*Physics Department and Center for High Energy and High Field Physics, National Central University (NCU), Tao Yuan, 32054, Taiwan*
[46]*INFN TIFPA, 38123 Trento, Italy*
[47]*Università di Trento, 38123 Trento, Italy*
[48]*Space Research Laboratory, Department of Physics and Astronomy, University of Turku, 20014 Turku, Finland*

(Received 14 August 2024; revised 31 October 2024; accepted 5 December 2024; published 3 February 2025)

We present results over an 11-year Solar cycle of cosmic antiprotons based on 1.1×10^6 events in the rigidity range from 1.00 to 41.9 GV. The $\bar{p}$ fluxes exhibit distinct properties. The magnitude of the $\bar{p}$ flux temporal variation is significantly smaller than those of p, e^-, and e^+. A hysteresis between the $\bar{p}$ fluxes and the p fluxes is observed, whereas the $\bar{p}$ and e^- fluxes show a linear correlation. With a model-independent analysis, we found a universal relation between the shape of the rigidity spectrum and the magnitude of flux temporal variation over an 11-year Solar cycle for both positively and negatively charged particles. The simultaneous results on $\bar{p}$ and p, e^-, and e^+ provide unique information for understanding particle transport in the Solar System as a function of mass, charge, and spectral shape.

DOI: 10.1103/PhysRevLett.134.051002

In this Letter, we present continuous antiproton $\bar{p}$ flux measurements per Bartels rotation (BR: 27 days) across an 11-year period from May 2011 to June 2022 in the rigidity range from 1.00 to 41.9 GV, based on 1.1×10^6 antiprotons collected by the Alpha Magnetic Spectrometer (AMS) on the International Space Station (ISS). Together with the AMS results on protons p, electrons e^-, and positrons e^+, these measurements of the time and rigidity dependence of charged elementary particles provide unique inputs for a comprehensive study of effects related to the solar magnetic field [1].

[*]Also at IRCCS Azienda Ospedaliero-Universitaria di Bologna, Bologna, Italy.
[†]Deceased.

The knowledge of the fluxes of charged elementary particles is crucial in understanding phenomena in the cosmos [2–4], such as the nature of dark matter. Experimental data on $\bar{p}$ are limited due to the low rate and overwhelming background; for each antiproton, there are approximately 10^4 protons. Since the first observation of antiprotons in cosmic rays [5], many studies on the antiproton flux and antiproton-to-proton flux ratio have been performed at different times and time intervals [6–13]. The AMS measurements of the cosmic antiproton flux [14,15] have generated widespread discussions about their origins [16].

The fluxes of charged cosmic rays outside the heliosphere are thought to be stable on the timescale of decades [17–21]. Time-dependent variations in galactic cosmic-ray fluxes measured inside the heliosphere are expected only due to solar modulation [1]. Solar modulation involves convective, diffusive, particle drift, and adiabatic energy loss processes [22,23]. The modulation effect depends on the rigidity, charge sign, mass, and shape of the rigidity spectra outside the heliosphere [24–31]. In the force-field approximation and many other models [22–33], the modulation effect from the spectral shape originates from the energy losses of particles in the heliosphere. At a given rigidity, this process decreases the overall modulation effect if the flux is increasing with rigidity and increases the overall modulation effect if the flux is decreasing with rigidity [32,33].

Previously, AMS has reported short-term variations on the scale of days to months and long-term variations on the scale of years in the daily fluxes of protons [34], electrons [35], and positrons [36]. Antiprotons have an identical mass but the opposite charge sign as protons and a different mass but the same charge sign as electrons. In addition, the $\bar{p}$ flux has a unique spectral shape at low rigidity [6–15]. This information provides a distinct channel for understanding solar modulation effects [37–47]. Moreover, accurate knowledge of the solar modulation effects on antiproton fluxes is crucial for understanding the origin of antiprotons in the cosmos [7,48].

The data presented in this Letter cover the main portion of Solar cycle 24, including the polarity reversal of the solar magnetic field in 2013 [49], and the beginning of Solar cycle 25. The simultaneous measurement of all four elementary particles provides comprehensive information for understanding solar modulation.

Detector—The layout and description of the AMS detector are presented in Refs. [15,50] and shown in Fig. S1 in Supplemental Material [51]. The key elements used in this measurement are the permanent magnet [52], the silicon tracker [53–55], the transition radiation detector (TRD) [56], the four planes of time of flight (TOF) scintillation counters [57], the ring imaging Čerenkov detector (RICH) [58], and the electromagnetic calorimeter (ECAL) [59,60]. More information on AMS layout, performance, trigger, and Monte Carlo simulation [61] is detailed in Supplemental Material [51].

Event selection—Over 2.0×10^{11} cosmic-ray events have been recorded in the first 11 years of AMS operations. In the rigidity range from 1.00 to 41.9 GV, we select antiproton samples using the combined information of TRD, TOF, RICH, silicon tracker, and ECAL. The details of the event selection, including the geomagnetic cutoff [62,63] and the backgrounds, are contained in Supplemental Material [51] and in Refs. [14,15]. After selection and background subtraction, we obtained 1.1×10^6 antiprotons.

Data analysis—The isotropic flux in the ith absolute rigidity bin $(R_i, R_i + \Delta R_i)$ for the jth time period is given by

$$\Phi_i^j = \frac{N_i^j}{A_i^j(1+\delta_i^j)\epsilon_i^j T_i^j \Delta R_i}, \tag{1}$$

where N_i^j is the number of events corrected for background and bin-to-bin migration using the unfolding procedure described in Ref. [64], A_i^j is the effective acceptance determined from the Monte Carlo simulation including geometric acceptance, event selection efficiencies, and interactions of antiprotons in the AMS materials, δ_i^j is the small correction to the acceptance due to the difference in selection efficiencies between data and Monte Carlo simulation, ϵ_i^j is the trigger efficiency, and T_i^j is the collection time (see Supplemental Material [51] for details). The antiproton flux for each Bartels rotation period is measured in 139 Bartels rotations from May 2011 to June 2022 in 11 rigidity bins from 1.00 to 41.9 GV.

The small corrections δ_i^j are estimated by comparing the efficiencies in data and Monte Carlo simulation of every selection cut using information from the detectors unrelated to that cut [14]. The δ_i^j are found to have a small rigidity dependence, smoothly varying from 8% at 1 GV to 3% at 10 GV.

Extensive studies of both time-dependent and time-independent systematic errors were performed. The major sources of systematic errors include the uncertainties in the background subtraction, the trigger efficiency, the geomagnetic cutoff, the acceptance calculation, the unfolding, and the absolute rigidity scale.

The uncertainty in background subtraction comprises two components: event selection and statistical fluctuation of the background template used to differentiate antiprotons from electrons and pions [14]. The systematic error due to event selection is 3.5% at 1 GV and 0.5% at 10 GV. The statistical fluctuation of the template affects the antiproton signal yield. This uncertainty is estimated by sampling the template according to the statistics and repeating the fitting, as well as by varying the fitting procedure. This error is 1.5% at 1 GV and less than 1% above 3 GV. These two components are independent and are added in quadrature.

The systematic error on antiproton fluxes associated with the trigger efficiency measurement is $< 1\%$ over the entire rigidity range and for every Bartels rotation.

The geomagnetic cutoff is calculated as described in Supplemental Material [51], and the resulting systematic error on the fluxes is about 2% at 1 GV and negligible (less than 0.4%) above 2 GV.

The systematic error of the effective acceptance is primarily due to the uncertainty in the interaction cross sections for antiprotons with the detector materials. It is independent of time and is 4% at 1 GV, decreasing smoothly to 2% above 20 GV [14]. The systematic error of the acceptance correction associated with the efficiency of selection and reconstruction is below 1%.

The systematic error associated with unfolding includes time-dependent and time-independent errors. The time-independent error comes from the uncertainty of the rigidity resolution function which has a pronounced Gaussian core and non-Gaussian tails. This error is obtained by repeating the unfolding procedure while independently varying the width of the Gaussian core by 5% and non-Gaussian tails by 20%. The resulting systematic error in the flux is 2.5% at 1 GV and decreases to less than 0.2% above 10 GV. The additional time-dependent systematic error in the unfolding procedure due to the variation of the antiproton spectral shape per Bartels rotation is about 4% at 1 GV and negligible (less than 0.3%) above 3 GV for all Bartels rotations.

The systematic error associated with the absolute rigidity scale has two sources. The first is due to residual tracker misalignment, and the second comes from the magnetic field map measurement with its temperature corrections [34]. The total time-independent systematic error on the fluxes due to uncertainty on the rigidity scale is less than 0.5% up to 41.9 GV.

The total systematic error is obtained by adding in quadrature the individual contributions of the time-independent systematic errors and the time-dependent systematic errors discussed above. For all Bartels rotations, at 1 GV it is about 9%, and above 5 GV it is about 4%.

Most importantly, several independent analyses were performed on the same data sample by different study groups. The results of those analyses are consistent with this Letter.

Results—The antiproton fluxes for each Bartels rotation, $\Phi_{\bar{p}}^{\mathrm{BR}}$, including statistical errors, time-dependent systematic errors, and total systematic errors are tabulated in Tables S1–S139 in Supplemental Material [51] as functions of rigidity at the top of the AMS detector. The time-averaged antiproton flux $\langle\Phi_{\bar{p}}\rangle$ over the 11-year Solar cycle is tabulated in Table S140 in Supplemental Material [51]. The tables are also provided in a machine-readable form [65]. The proton fluxes Φ_p, the electron fluxes Φ_{e^-}, and the positron fluxes Φ_{e^+} are taken from Refs. [34–36]. They are rebinned in order to compare with the antiproton data. The complete rebinned Φ_p, Φ_{e^-}, and Φ_{e^+} data up to June 2022 are provided in a machine-readable form [34–36].

Figure 1 presents the antiproton fluxes as a function of rigidity and as a function of time. The fluxes measured for each Bartels rotation ($\Phi_{\bar{p}}^{\mathrm{BR}}$) are presented in Fig. 1(a) below 2.97 GV, where the fluxes increase with increasing rigidity, and above 2.97 GV in Fig. 1(b), where the fluxes decrease with increasing rigidity. To examine the 11-year variations of the antiproton fluxes, Figs. 1(c) and 1(d) present the $\Phi_{\bar{p}}$ using their 13-BR moving average with a step of 1 BR for the same rigidities as in Figs. 1(a) and 1(b), respectively. As seen, $\Phi_{\bar{p}}$ exhibit distinct properties as a function of time. Below ~10 GV, $\Phi_{\bar{p}}$ exhibit significant temporal variation and the relative magnitudes of the flux variations decrease with increasing rigidity. Figures 1(e) and 1(f) present the three-dimensional variation of $\Phi_{\bar{p}}$ as functions of time and rigidity. Figure S2 in Supplemental Material [51] shows $\langle\Phi_{\bar{p}}\rangle$ together with other measurements collected over much shorter time intervals [6–13]. As seen, $\langle\Phi_{\bar{p}}\rangle$ exhibits distinct properties as a function of rigidity: From 1 to 2 GV the flux increases with rigidity, from 2 to 4 GV the flux reaches a maximum and turns over at ≈3 GV, and from 4 GV the flux continues to decrease.

Figure 2 presents the fluxes of elementary particles measured by AMS in the 11-year period. Figure 2(a) shows the time-averaged fluxes $\langle\Phi_p\rangle$, $\langle\Phi_{e^-}\rangle$, $\langle\Phi_{e^+}\rangle$, and $\langle\Phi_{\bar{p}}\rangle$ as a function of rigidity. As seen, the rigidity dependence of $\langle\Phi_{\bar{p}}\rangle$ is distinctly different from that of the other fluxes which all decrease with increasing rigidity. The ranges of flux temporal variation during this period are presented as shaded bands. Figure S3 in Supplemental Material [51] presents the temporal evolution of all elementary particle fluxes for four characteristic rigidity bins using their 13-BR moving average values. As seen, below ≈4 GV, the magnitude of the $\Phi_{\bar{p}}$ temporal variation is significantly smaller compared to that of the other fluxes. All four fluxes reach a minimum around 2014–2015 and a maximum around 2020. Figures 2(b)–2(g) present the temporal evolution of Φ_p, Φ_{e^-}, Φ_{e^+}, and $\Phi_{\bar{p}}$ in the rigidity range [1.00–1.92] GV. As seen, all four fluxes exhibit complex temporal structures. However, the temporal structures of $\Phi_{\bar{p}}$ are distinctly different from that of the other elementary particle fluxes. Figures 2(b) and 2(c) compare particles with opposite charge but identical mass. As seen, the difference in the temporal variation between $\Phi_{\bar{p}}$ and Φ_p is much greater than between Φ_{e^-} and Φ_{e^+}. Similarly, Figs. 2(d) and 2(e) compare particles with identical charge but different masses. As seen, the difference in the temporal variation between Φ_{e^-} and $\Phi_{\bar{p}}$ is much larger than that between Φ_{e^+} and Φ_p, despite the same difference in mass. Figures 2(f) and 2(g) compare the fluxes of antiparticles and particles. As seen, the difference in the temporal variations between $\Phi_{\bar{p}}$ and Φ_{e^+} is also distinct from that between Φ_p and Φ_{e^-}. These observations indicate the important modulation effects of the spectral shape, in

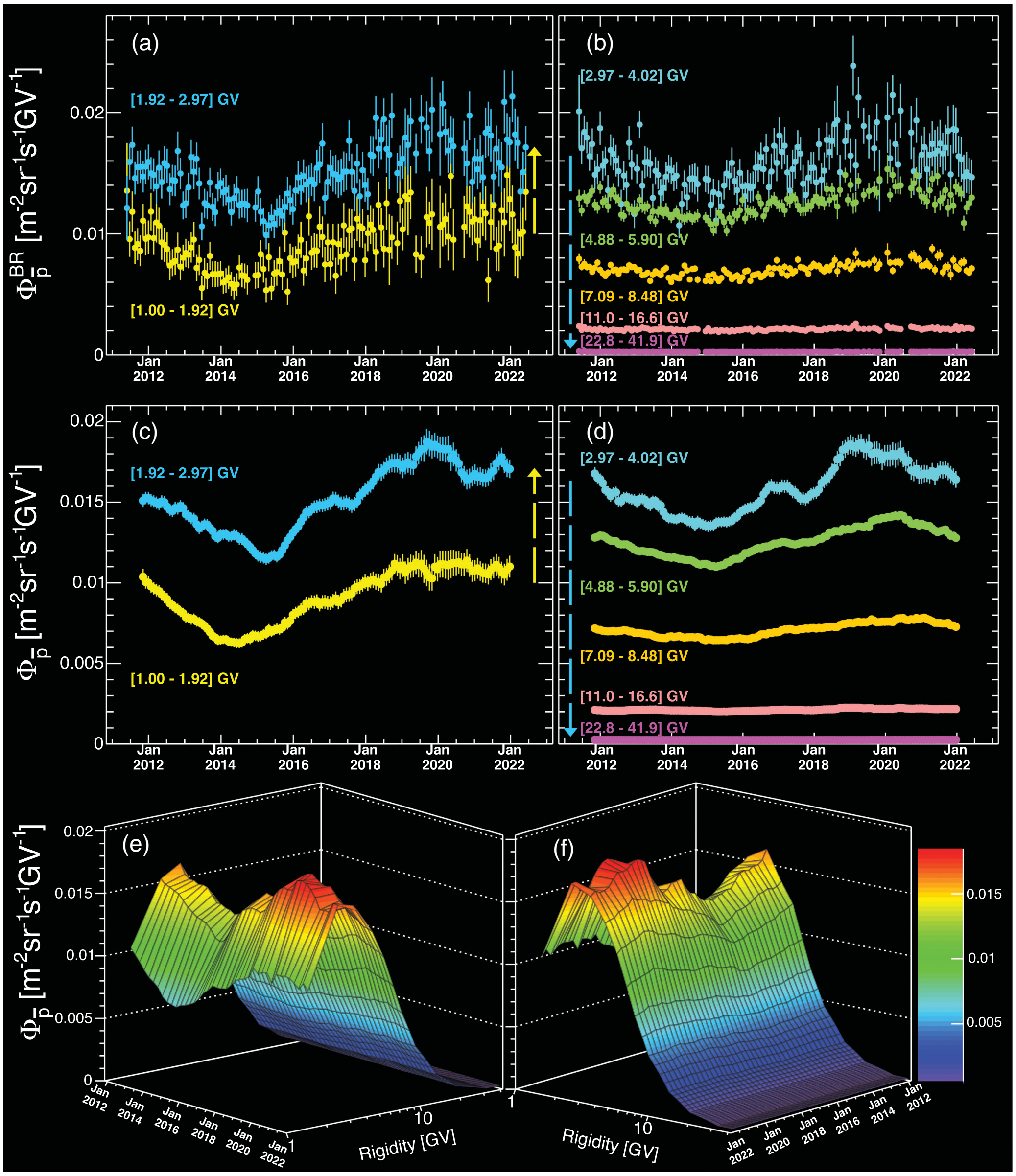

FIG. 1. Temporal evolution of $\Phi_{\bar{p}}^{\mathrm{BR}}$ for (a) below 2.97 GV where the fluxes $\Phi_{\bar{p}}^{\mathrm{BR}}$ increase with increasing rigidity and (b) above 2.97 GV where the fluxes $\Phi_{\bar{p}}^{\mathrm{BR}}$ decrease with increasing rigidity, as indicated by the arrows. (c) and (d) present the $\Phi_{\bar{p}}$ using their 13-BR moving average values. The data point for each Bartels rotation period is calculated from a time window of 13 BR centered around that period, taking into account the correlation in the systematic errors. In (a)–(d), the error bars are the quadratic sum of the statistical and time-dependent systematic errors. As seen, over a Solar cycle of 11 years, $\Phi_{\bar{p}}$ exhibit significant temporal variation up to ~10 GV and the relative magnitudes of the flux temporal variations decrease with increasing rigidity. Above ~10 GV, the flux variations are not visible. In (e) and (f), the three-dimensional variation of $\Phi_{\bar{p}}$ as functions of time and rigidity is shown.

addition to the modulation effects from particle mass and charge sign.

The long-term variations on the scale of years are related to the 11- and 22-year cycles of the solar magnetic field [1]. Previously, AMS studied the differences in the modulation of Φ_p, Φ_{e^-}, and Φ_{e^+}, using their correlation in time and observed a hysteresis behavior between Φ_{e^-} and Φ_p [35] and Φ_{e^-} and Φ_{e^+} [36], but a linear relation between Φ_{e^+} and Φ_p [36]. With the antiproton results, AMS is able to study the correlation among all four elementary particle fluxes and measure the differences in their modulation. Figure 3 summarizes the flux correlations between elementary particles in the rigidity range [1.00–2.97] GV [34–36].

As seen in Fig. 3(a), $\Phi_{\bar{p}}$ and Φ_p exhibit a hysteresis behavior, such that, at a given Φ_p, $\Phi_{\bar{p}}$ shows two distinct branches over time, one before 2014–2015 and one after. This behavior is similar to the hysteresis behavior between Φ_{e^-} and Φ_{e^+} shown in Fig. 3(b). The hysteresis behavior

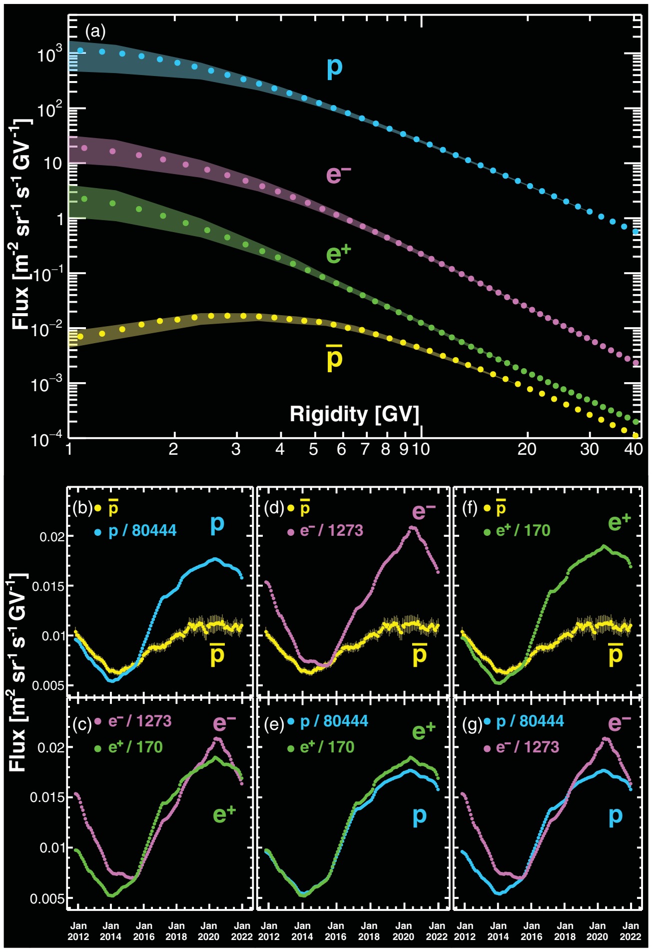

FIG. 2. (a) The 11-year time-averaged fluxes of $\langle\Phi_{\bar{p}}\rangle$ (yellow points), $\langle\Phi_{e^+}\rangle$ (green points), $\langle\Phi_{e^-}\rangle$ (magenta points), and $\langle\Phi_p\rangle$ (blue points). The ranges of the flux temporal variation during this period are shown as shaded bands. In (b)–(g), the temporal evolutions of cosmic elementary particle fluxes in the rigidity range 1.00–1.92 GV for $\Phi_{\bar{p}}$ (yellow points), Φ_p (blue points), Φ_{e^+} (green points), and Φ_{e^-} (magenta points) are compared. As seen, all four fluxes exhibit complex temporal structures, and $\Phi_{\bar{p}}$ is distinctly different from all other elementary particle fluxes. For (b)–(g), each data point represents the 13-BR moving average flux. Φ_p, Φ_{e^+}, and Φ_{e^-} are scaled as indicated such that all fluxes are of the same magnitude on average during 2015.

between $\Phi_{\bar{p}}$ and Φ_p is studied following the method described in Ref. [35] and is compared with the hysteresis behavior between Φ_{e^-} and Φ_{e^+} as detailed in Supplemental Material [51]. As seen in Fig. S4, in each rigidity bin below 11.0 GV, a hysteresis between $\Phi_{\bar{p}}$ and Φ_p is observed. The hysteresis behavior between particles with identical mass but opposite charge sign shows a clear charge-sign effect in the solar modulation. Furthermore, as seen in Table SA and Fig. S5, below 4.88 GV the detailed hysteresis behavior between $\Phi_{\bar{p}}$ and Φ_p is different from the hysteresis behavior between Φ_{e^-} and Φ_{e^+} by more than 4σ significance.

Figure 3(c) shows a linear relation between $\Phi_{\bar{p}}$ and Φ_{e^-}. This behavior is similar to the linear relation between Φ_p and Φ_{e^+} shown in Fig. 3(d). The relation between $\Phi_{\bar{p}}$ and Φ_{e^-} is analyzed as described in Supplemental Material [51] and presented in Figs. S6 and S7. As seen, the linear relation between $\Phi_{\bar{p}}$ and Φ_{e^-} is observed for all rigidity bins between 1.00 and 7.09 GV, where $\Phi_{\bar{p}}$ is modulated significantly less than Φ_{e^-}. In comparison, the linear relation between Φ_p and Φ_{e^+} shows that their temporal variations are more similar, while Φ_p is also modulated less than Φ_{e^+} [36]. These observations show that particles with the same charge sign are modulated similarly but with differences in their temporal variation originating from mass and spectral shape. Since the difference in mass between p and e^+ is the same as between $\bar{p}$ and e^-, the difference between the linear relations of $\Phi_{\bar{p}}$ versus Φ_{e^-} and Φ_p versus Φ_{e^+}, as seen in Figs. 3(c) and 3(d) and in Fig. S7, shows the importance of the spectral shape in solar modulation.

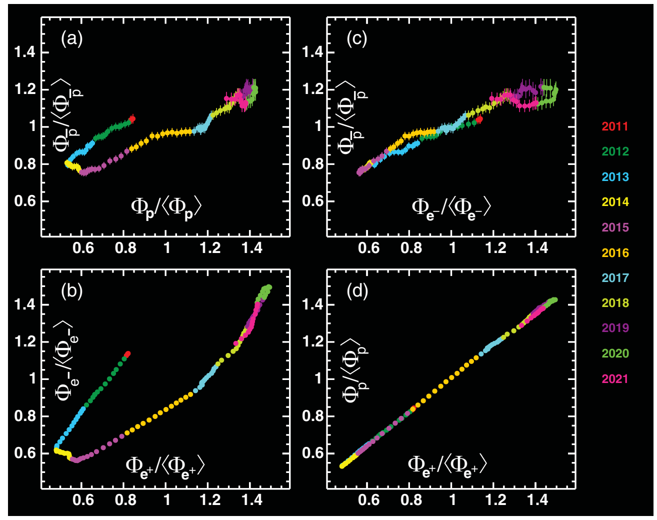

FIG. 3. Correlation between elementary particle fluxes in the rigidity range from 1.00 to 2.97 GV for (a) $\Phi_{\bar{p}}$ and Φ_p, (b) Φ_{e^-} and Φ_{e^+}, (c) $\Phi_{\bar{p}}$ and Φ_{e^-}, and (d) Φ_p and Φ_{e^+}. The data points correspond to flux values of 13-BR moving averages and are normalized to their respective time-averaged value $\langle\Phi\rangle$ over the 11-year period. Different colors indicate different years. As seen in (a) and (b), the flux correlations between particles with opposite charge sign but identical mass exhibit distinct hysteresis behaviors. In contrast, (c) and (d) show that the flux correlations between particles with the same charge sign but different masses exhibit linear relations. Note that, in (a) and (c), the fine structures within the timescale of one year are mostly due to the statistical fluctuations of $\Phi_{\bar{p}}$ and are not significant. Note that in this figure the horizontal error bars are smaller than the symbols.

To study the modulation effects from the spectral shape, we perform a model-independent analysis using the spectral indices of the 11-year time-averaged fluxes and the magnitude of flux temporal variation. The spectral indices γ of elementary particle fluxes are determined from

$$\gamma = d[\log(\Phi)]/d[\log(R)]. \tag{2}$$

Figure S8 in Supplemental Material [51] shows the spectral indices for $\bar{p}(\gamma_{\bar{p}})$, $p(\gamma_p)$, $e^-(\gamma_{e^-})$, and $e^+(\gamma_{e^+})$ as a function of rigidity. They are determined from the 11-year time-averaged fluxes using sliding rigidity windows of 5–7 bins chosen to have sufficient sensitivity to the spectral index. As seen, $\gamma_{\bar{p}}$ exhibits distinct behavior compared to other particles. Below ≈ 3 GV, $\gamma_{\bar{p}} > 0$, that is, the antiproton fluxes increase with increasing rigidity. For each rigidity bin, $\gamma_{\bar{p}} > \gamma_{e^-}$ and $\gamma_p > \gamma_{e^+}$, but the difference between $\gamma_{\bar{p}}$ and γ_{e^-} is much larger than that between γ_p and γ_{e^+}.

To quantify the flux variation range over this 11-year Solar cycle, for each particle and in each rigidity bin, the 13-BR moving average fluxes are used to define the relative magnitude of the flux variation (M) as the ratio between the maximum flux value and the minimum flux value over the 11-year period. Figure S9 in Supplemental Material [51] presents the magnitude of flux temporal variations for $\bar{p}(M_{\bar{p}})$, $p(M_p)$, $e^-(M_{e^-})$, and $e^+(M_{e^+})$ as a function of rigidity. As seen, below 4.02 GV, $M_{\bar{p}}$ is much smaller than others. Furthermore, $M_{\bar{p}} < M_{e^-}$ and $M_p < M_{e^+}$, but the difference between $M_{\bar{p}}$ and M_{e^-} is larger than that between M_p and M_{e^+}.

Figure 4(a) presents M versus γ for negatively charged particles $\bar{p}$ and e^- and positively charged particles p and e^+. Remarkably, for each rigidity bin, M versus γ exhibits the same dependence for negatively and positively charged particles as indicated by the dashed lines. As seen, $M_{\bar{p}} < M_{e^-}$ while $\gamma_{\bar{p}} > \gamma_{e^-}$, and $M_p < M_{e^+}$ while $\gamma_p > \gamma_{e^+}$. Figure 4(b) shows the ratios of the difference in M (ΔM) to the difference in γ ($\Delta\gamma$) between negatively charged particles e^- and $\bar{p}$ [$\Delta M(e^-,\bar{p})/\Delta\gamma(e^-,\bar{p})$] and between positively charged particles e^+ and p [$\Delta M(e^+,p)/\Delta\gamma(e^+,p)$] up to 11 GV. As seen, the ratios are less than zero; that is, the flux with a larger spectral index has a smaller variation magnitude. The ratios approach zero with increasing rigidity, indicating that the influence of the spectral shape on flux variation magnitude is decreasing with increasing rigidity. Most importantly, the ratios determined from positively and negatively charged particles are the same within the errors, revealing a universal relation between flux variation magnitude and spectral index, independent of the charge sign. This universal relation shows that the differences in modulation between $\bar{p}$ and e^- and between p and e^+ are mainly due to the difference in their spectral shape. These results on the effect of spectral shape in solar modulation provide crucial input to understand the antiproton local interstellar spectrum.

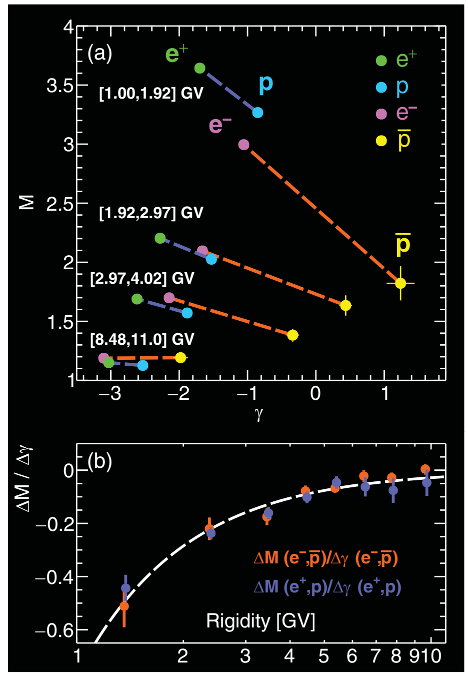

FIG. 4. (a) The magnitude of flux temporal variation M versus the spectral index γ of $\bar{p}$ (yellow points), e^- (magenta points), p (light blue points), and e^+ (green points), for four typical rigidity bins. For each rigidity bin, the dashed lines connect particles with the same charge sign and show the dependence between M and γ. As seen, the dependence is the same for (e^-, $\bar{p}$) and for (e^+, p): $M_{\bar{p}} < M_{e^-}$ while $\gamma_{\bar{p}} > \gamma_{e^-}$ (orange lines), and $M_p < M_{e^+}$ while $\gamma_p > \gamma_{e^+}$ (dark blue lines). (b) The ratios of the difference in M (ΔM) to the difference in γ ($\Delta\gamma$) between e^- and $\bar{p}$ [$\Delta M(e^-,\bar{p})/\Delta\gamma(e^-,\bar{p})$, orange points] and between e^+ and p [$\Delta M(e^+,p)/\Delta\gamma(e^+,p)$, dark blue points] as a function of rigidity. As seen, $\Delta M(e^-,\bar{p})/\Delta\gamma(e^-,\bar{p})$ and $\Delta M(e^+,p)/\Delta\gamma(e^+,p)$ are the same within the errors, revealing a universal relation independent of the charge sign. In (b), the horizontal positions for $\Delta M(e^+,p)/\Delta\gamma(e^+,p)$ are displaced slightly for clarity. The white dashed curve is to guide the eye.

In conclusion, we presented the AMS measurements over an 11-year Solar cycle of cosmic antiprotons based on 1.1×10^6 events in the rigidity range from 1.00 to 41.9 GV. The temporal variations of the fluxes of all cosmic charged elementary particles, $\bar{p}$, p, e^-, and e^+, are studied simultaneously. Compared to p, e^-, and e^+, the $\bar{p}$ fluxes exhibit distinct properties. The magnitude of the $\bar{p}$ flux temporal variation is significantly smaller than those of p, e^-, and e^+. A hysteresis between the $\bar{p}$ fluxes and the p fluxes is observed, whereas the $\bar{p}$ and e^- fluxes show a linear correlation. With a model-independent analysis, we found a universal relation between the shape of the rigidity spectrum and the magnitude of flux temporal variation over an 11-year Solar cycle, independent of the charge sign. These results provide unique information for understanding solar modulation as a function of mass, charge, and spectral shape and essential inputs for the understanding of the origin of antiprotons in the cosmos.

Acknowledgments—We are grateful for important physics discussions with Igor Moskalenko. We thank former NASA Administrator Daniel S. Goldin for his dedication to the legacy of the ISS as a scientific laboratory and his decision for NASA to fly AMS as a DOE payload. We also acknowledge the continuous support of the NASA leadership, particularly Ken Bowersox and of the JSC and MSFC flight control teams that have allowed AMS to operate optimally on the ISS for over 13 years. We are grateful for the support of Regina Rameika and Glen Crawford of the DOE including resources from the National Energy Research Scientific Computing Center under Contract No. DE-AC02-05CH11231. We gratefully acknowledge the strong support from CERN, including Fabiola Gianotti, and the CERN IT department, including Bernd Panzer-Steindel. We also acknowledge the continuous support from MIT and its School of Science, Nergis Mavalvala, and the Laboratory for Nuclear Science, Boleslaw Wyslouch. Research supported by Chinese Academy of Sciences, Institute of High Energy Physics, National Natural Science Foundation (NSFC), and Ministry of Science and Technology, National Key R&D Program Grants No. 2022YFA1604802 and No. 2022YFA1604803, NSFC Grant No. 12275158, the China Scholarship Council, the provincial governments of Shandong, Jiangsu, Guangdong, Shandong University, and the Shandong Institute of Advanced Technology, China; Research Council of Finland, Project No. 321882, and Finnish Academy of Sciences and Letters, Grant No. 301123, Finland; CNRS/IN2P3 and CNES, France; DLR under Grant No. 50OO1803 and computing support on the JARA Partition of the RWTH Aachen supercomputer, Germany; INFN and ASI under ASI-INFN Agreement No. 2019-19-HH.0, its amendments, No. 2021-43-HH.0, and ASI-University of Perugia Agreement No. 2019-2-HH.0, and the Italian Ministry of University and Research (MUR) through the program *"Dipartimenti di Eccellenza 2023–2027"* (Grant SUPER-C), Italy; the Consejo Nacional de Humanidades, Ciencias y Tecnologías (CONAHCYT) under Grant No. CF-2019/2042 and UNAM, Mexico; NWO under Grant No. 680-1-004, Netherlands; FCT under Grant No. CERN/FIS-PAR/0013/2019, Portugal; CIEMAT, IAC, CDTI, MCIN-AEI, and ERDF under Grants No. PID2022-137810NB-C21/C22, No. PCI2023-145945-2, No. PCI2023-145961-2, No. CEX2019-000920-S, and No. JDC2022-049705-I, Spain; the Fondation Dr. Manfred Steuer, Switzerland; Academia Sinica, the National Science and Technology Council (NSTC), formerly the Ministry of Science and Technology (MOST), under Grants No. 111-2123-M-001-004 and No. 111-2112-M-006-029, High Education Sprout Project by the Ministry of Education at National Cheng Kung University, former Presidents of Academia Sinica Yuan-Tseh Lee and Chi-Huey Wong and former Ministers of NSTC (formerly MOST) Maw-Kuen Wu and Luo-Chuan Lee, Taiwan; the Turkish Energy, Nuclear and Mineral Research Agency (TENMAK) under Grant No. 2020TAEK(CERN)A5.H1.F5-26, Türkiye; and NSF Grant No. 2013228 and ANSWERS proposals No. 2149809, No. 2149810, and No. 2149811, LWS NASA Grant/Cooperative Agreement No. 80NSSC20K1819, and FINESST NASA Grant No. 80NSSC21K1392, USA.

[1] M. S. Potgieter, Solar modulation of cosmic rays, Living Rev. Solar Phys. **10**, 3 (2013).

[2] M. S. Turner and F. Wilczek, Positron line radiation as a signature of particle dark matter in the halo, Phys. Rev. D **42**, 1001 (1990); J. Ellis, Particles and cosmology: Learning from cosmic rays, AIP Conf. Proc. **516**, 21 (2000); F. Donato, N. Fornengo, and P. Salati, Antideuterons as a signature of supersymmetric dark matter, Phys. Rev. D **62**, 043003 (2000); H. C. Cheng, J. L. Feng, and K. T. Matchev, Kaluza-Klein dark matter, Phys. Rev. Lett. **89**, 211301 (2002); M. Cirelli, R. Franceschini, and A. Strumia, Minimal dark matter predictions for galactic positrons, anti-protons, photons, Nucl. Phys. **B800**, 204 (2008); C. Evoli, I. Cholis, D. Grasso, L. Maccione, and P. Ullio, Antiprotons from dark matter annihilation in the Galaxy: Astrophysical uncertainties, Phys. Rev. D **85**, 123511 (2012); M. Garny, A. Ibarra, and S. Vogl, Dark matter annihilations into two light fermions and one gauge boson: General analysis and antiproton constraints, J. Cosmol. Astropart. Phys. 04 (2012) 033; T. Delahaye and M. Grefe, Antiproton limits on decaying gravitino dark matter, J. Cosmol. Astropart. Phys. 12 (2013) 045; J. Kopp, Constraints on dark matter annihilation from AMS-02 results, Phys. Rev. D **88**, 076013 (2013); C. H. Chen, C. W. Chiang, and T. Nomura, Dark matter for excess of AMS-02 positrons and antiprotons, Phys. Lett. B **747**, 495 (2015); H. C. Cheng, W. C. Huang, X. Huang, I. Low, Y. L. Sming Tsai, and Q. Yuan, AMS-02 positron excess and indirect detection of three-body decaying dark matter, J. Cosmol. Astropart. Phys. 03 (2017) 041; Y. Bai, J. Berger, and S. Lu, Supersymmetric resonant dark matter: A thermal model for the AMS-02 positron excess, Phys. Rev. D **97**, 115012 (2018).

[3] P. D. Serpico, Astrophysical models for the origin of the positron "excess", Astropart. Phys. **39–40**, 2 (2012); T. Linden and S. Profumo, Probing the pulsar origin of the anomalous positron fraction with AMS-02 and atmospheric Cherenkov telescopes, Astrophys. J. **772**, 18 (2013); I. Cholis and D. Hooper, Dark matter and pulsar origins of the rising cosmic ray positron fraction in light of new data from the AMS, Phys. Rev. D **88**, 023013 (2013); D. Hooper, I. Cholis, T. Linden, and K. Fang, HAWC observations strongly favor pulsar interpretations of the cosmic-ray positron excess, Phys. Rev. D **96**, 103013 (2017); S. Profumo, J. Reynoso-Cordova, N. Kaaz, and M. Silverman, Lessons from HAWC pulsar wind nebulae observations: The diffusion constant is not a constant; pulsars remain the likeliest sources of the anomalous positron fraction; cosmic rays are trapped for long periods of time in pockets of inefficient diffusion, Phys. Rev. D **97**, 123008 (2018).

[4] T. Shibata, Y. Futo, and S. Sekiguchi, Antiprotons and cosmic-ray propagation in the Galaxy, Astrophys. J. **678**, 907 (2008); P. Blasi, Origin of the positron excess in cosmic

rays, Phys. Rev. Lett. **103**, 051104 (2009); K. Blum, B. Katz, and E. Waxman, AMS-02 results support the secondary origin of cosmic ray positrons, Phys. Rev. Lett. **111**, 211101 (2013); R. Cowsik, B. Burch, and T. Madziwa-Nussinov, The origin of the spectral intensities of cosmic-ray positrons, Astrophys. J. **786**, 124 (2014); P. Lipari, Interpretation of the cosmic ray positron and antiproton fluxes, Phys. Rev. D **95**, 063009 (2017); I. Cholis, D. Hooper, and T. Linden, Possible evidence for the stochastic acceleration of secondary antiprotons by supernova remnants, Phys. Rev. D **95**, 123007 (2017).

[5] E. A. Bogomolov, N. D. Lubyanaya, V. A. Romanov, S. V. Stepanov, and M. S. Shulakova, A stratospheric magnetic spectrometer investigation of the singly charged component spectra and composition of the primary and secondary cosmic radiation, *Proceedings of the 16th International Cosmic Ray Conference* (1979), Vol. 1, p. 330; R. L. Golden, S. Horan, B. G. Mauger, G. D. Badhwar, J. L. Lacy, S. A. Stephens, R. R Daniel, and J. E. Zipse, Evidence for the existence of cosmic-ray antiprotons, Phys. Rev. Lett. **43**, 1196 (1979); A. Buffington and S. M. Shindler, Recent cosmic-ray antiproton measurements and astrophysical implications, Astrophys. J. **247**, L105 (1981).

[6] M. H. Salamon *et al.*, Limits on the antiproton/proton ratio in the cosmic radiation from 100 MeV to 1580 MeV, Astrophys. J. **349**, 78 (1990).

[7] K. Yoshimura *et al.*, Observation of cosmic-ray antiprotons at energies below 500 MeV, Phys. Rev. Lett. **75**, 3792 (1995); S. Orito *et al.*, Precision measurement of cosmic-ray antiproton spectrum, Phys. Rev. Lett. **84**, 1078 (2000); T. Maeno *et al.*, Successive measurements of cosmic-ray antiproton spectrum in a positive phase of the Solar cycle, Astropart. Phys. **16**, 121 (2001); Y. Asaoka *et al.*, Measurements of cosmic-ray low-energy antiproton and proton spectra in a transient period of solar field reversal, Phys. Rev. Lett. **88**, 051101 (2002); K. Abe *et al.*, Measurement of the cosmic-ray low-energy antiproton spectrum with the first BESS-Polar Antarctic flight, Phys. Lett. B **670**, 103 (2008); K. Abe *et al.*, Measurement of the cosmic-ray antiproton spectrum at solar minimum with a long-duration balloon flight over antarctica, Phys. Rev. Lett. **108**, 051102 (2012); A. Yamamoto *et al.*, Search for cosmic-ray antiproton origins and for cosmological antimatter with BESS, Adv. Space Res. **51**, 227 (2013); K. Abe *et al.*, The results from BESS-Polar experiment, Adv. Space Res. **60**, 806 (2017).

[8] J. W. Mitchell *et al.*, Measurement of 0.25–3.2 GeV antiprotons in the cosmic radiation, Phys. Rev. Lett. **76**, 3057 (1996).

[9] M. Hof *et al.*, Measurement of cosmic-ray antiprotons from 3.7 to 19 GeV, Astrophys. J. **467**, L33 (1996).

[10] M. Boezio *et al.*, The cosmic-ray antiproton flux between 0.62 and 3.19 GeV measured near solar minimum activity, Astrophys. J. **487**, 415 (1997); M. Boezio *et al.*, The cosmic-ray antiproton flux between 3 and 49 GeV, Astrophys. J. **561**, 787 (2001).

[11] A. S. Beach *et al.*, Measurement of the cosmic-ray antiproton-to-proton abundance ratio between 4 and 50 GeV, Phys. Rev. Lett. **87**, 271101 (2001).

[12] M. Aguilar *et al.*, The Alpha Magnetic Spectrometer (AMS) on the International Space Station: Part I—results from the test flight on the space shuttle, Phys. Rep. **366**, 331 (2002).

[13] O. Adriani *et al.*, New measurement of the antiproton-to-proton flux ratio up to 100 GeV in the cosmic radiation, Phys. Rev. Lett. **102**, 051101 (2009); O. Adriani *et al.*, PAMELA results on the cosmic-ray antiproton flux from 60 MeV to 180 GeV in kinetic energy, Phys. Rev. Lett. **105**, 121101 (2010); O. Adriani *et al.*, Measurement of the flux of primary cosmic ray antiprotons with energies of 60 MeV to 350 GeV in the PAMELA experiment, JETP Lett. **96**, 621 (2013).

[14] M. Aguilar *et al.*, Antiproton flux, antiproton-to-proton flux ratio, and properties of elementary particle fluxes in primary cosmic rays measured with the Alpha Magnetic Spectrometer on the International Space Station, Phys. Rev. Lett. **117**, 091103 (2016).

[15] M. Aguilar *et al.*, The Alpha Magnetic Spectrometer (AMS) on the International Space Station: Part II—Results from the first seven years, Phys. Rep. **894**, 1 (2021).

[16] K. Hamaguchi, T. Moroi, and K. Nakayama, AMS-02 antiprotons from annihilating or decaying dark matter, Phys. Lett. B **747**, 523 (2015); Y.-H. Chen, K. Cheung, and P.-Y. Tseng, Dark matter with multiannihilation channels and the AMS-02 positron excess and antiproton data, Phys. Rev. D **93**, 015015 (2016); R. Cowsik and T. Madziwa-Nussinov, Spectral intensities of antiprotons and the nested leaky-box model for cosmic rays in the galaxy, Astrophys. J. **827**, 119 (2016); A. Cuoco, M. Krämer, and M. Korsmeier, Novel dark matter constraints from antiprotons in light of AMS-02, Phys. Rev. Lett. **118**, 191102 (2017); M.-Y. Cui, Q. Yuan, Y.-L. S. Tsai, and Y.-Z. Fan, Possible dark matter annihilation signal in the AMS-02 antiproton data, Phys. Rev. Lett. **118**, 191101 (2017); Q. Yuan, S.-J. Lin, K. Fang, and X.-J. Bi, Propagation of cosmic rays in the AMS-02 era, Phys. Rev. D **95**, 083007 (2017); M. W. Winkler, Cosmic ray antiprotons at high energies, J. Cosmol. Astropart. Phys. 02 (2017) 048; K. Blum, R. Sato, and M. Takimoto, e^+ and $\bar{p}$ production in pp collisions and the cosmic-ray $e^+/\bar{p}$ ratio, Phys. Rev. D **98**, 063022 (2018); A. Reinert and M. W. Winkler, A precision search for WIMPs with charged cosmic rays, J. Cosmol. Astropart. Phys. 01 (2018) 055; A Cuoco, J. Heisig, L. Klamt, M. Korsmeier, and M. Krämer, Scrutinizing the evidence for dark matter in cosmic-ray antiprotons, Phys. Rev. D **99**, 103014 (2019); I. Cholis, T. Linden, and D. Hooper, A robust excess in the cosmic-ray antiproton spectrum: Implications for annihilating dark matter, Phys. Rev. D **99**, 103026 (2019); M. Carena, J. Osborne, N. R. Shah, and C. E. M. Wagner, Return of the WIMP: Missing energy signals and the Galactic Center excess, Phys. Rev. D **100**, 055002 (2019); V. Bresci, E. Amato, P. Blasi, and G. Morlino, Effects of re-acceleration and source grammage on secondary cosmic rays spectra, Mon. Not. R. Astron. Soc. **488**, 2068 (2019); H.-B. Jin, Y.-L Wu, and Y.-F. Zhou, Astrophysical background and dark matter implication based on latest AMS-02 data, Astrophys. J. **901**, 80 (2020); P. Mertsch, A. Vittino, and S. Sarkar, Explaining cosmic ray antimatter with secondaries from old supernova remnants, Phys. Rev. D **104**, 103029 (2021).

[17] M. Simon, A. Molnar, and S. Roesler, A new calculation of the interstellar secondary cosmic-ray antiprotons, Astrophys. J. **499**, 250 (1998).

[18] A. W. Strong and I. V. Moskalenko, Propagation of cosmic-ray nucleons in the galaxy, Astrophys. J. **509**, 212 (1998); A. E. Vladimirov, S. W. Digel, G. Jóhannesson, P. F. Michelson, I. V. Moskalenko, P. L. Nolan, E. Orlando, T. A. Porter, and A. W. Strong, GALPROP WebRun: An internet-based service for calculating galactic cosmic ray propagation and associated photon emissions, Comput. Phys. Commun. **182**, 1156 (2011); G. Jóhannesson, R. Ruiz de Austri, A. C. Vincent, I. V. Moskalenko, E. Orlando, T. A. Porter, A. W. Strong, R. Trotta, F. Feroz, P. Graff, and M. P. Hobson, Bayesian analysis of cosmic ray propagation: Evidence against homogeneous diffusion, Astrophys. J. **824**, 16 (2016).

[19] C. Evoli, D. Gaggero, A. Vittino, G. Di Bernardo, M. Di Mauro, A. Ligorini, P. Ullio, and D. Grasso, Cosmic-ray propagation with DRAGON2: I. Numerical solver and astrophysical ingredients, J. Cosmol. Astropart. Phys. 02 (2017) 015.

[20] D. Maurin, F. Donato, R. Taillet, and P. Salati, Cosmic rays below $Z = 30$ in a diffusion model: New constraints on propagation parameters, Astrophys. J. **555**, 585 (2001).

[21] A. Putze, L. Derome, and D. Maurin, A Markov Chain Monte Carlo technique to sample transport and source parameters of Galactic cosmic rays II. Results for the diffusion model combining B/C and radioactive nuclei, Astron. Astrophys. **516**, A66 (2010).

[22] E. N. Parker, The passage of energetic charged particles through interplanetary space, Planet. Space Sci. **13**, 9 (1965).

[23] L. J. Gleeson and W. I. Axford, Solar modulation of galactic cosmic rays, Astrophys. J. **154**, 1011 (1968).

[24] M. S. Potgieter, The charge-sign dependent effect in the solar modulation of cosmic rays, Adv. Space Res. **53**, 1415 (2014).

[25] L. Maccione, Low energy cosmic ray positron fraction explained by charge-sign dependent solar modulation, Phys. Rev. Lett. **110**, 081101 (2013).

[26] M. J. Boschini, S. D. Torre, M. Gervasi, D. Grandi, G. Jóhannesson, M. Kachelriess, G. L. Vacca, N. Masi, I. V. Moskalenko, and E. Orlando, Solution of heliospheric propagation: Unveiling the local interstellar spectra of cosmic-ray species, Astrophys. J. **840**, 115 (2017).

[27] M. Kuhlen and P. Mertsch, Time-dependent AMS-02 electron-positron fluxes in an extended force-field model, Phys. Rev. Lett. **123**, 251104 (2019).

[28] I. Cholis, D. Hooper, and T. Linden, A predictive analytic model for the solar modulation of cosmic rays, Phys. Rev. D **93**, 043016 (2016); I. Cholis, D. Hooper, and T. Linden, Constraining the charge-sign and rigidity-dependence of solar modulation, J. Cosmol. Astropart. Phys. 10 (2022) 051; I. Cholis and I. McKinnon, Constraining the charge-, time-, and rigidity-dependence of cosmic-ray solar modulation with AMS-02 observations during Solar Cycle 24, Phys. Rev. D **106**, 063021 (2022).

[29] X. Song, X. Luo, M. S. Potgieter, and M. Zhang, Comprehensive modulation potential for the solar modulation of Galactic cosmic rays, Phys. Rev. D **106**, 123004 (2022).

[30] N. Eugene Engelbrecht, F. Effenberger, V. Florinski, M. S. Potgieter, D. Ruffolo, R. Chhiber, A. V. Usmanov, J. S. Rankin, and P. L. Els, Theory of cosmic ray transport in the heliosphere, Space Sci. Rev. **218**, 33 (2022).

[31] O. P. M. Aslam, X. Luo, M. S. Potgieter, M. D. Ngobeni, and X. Song, Unfolding drift effects for cosmic rays over the period of the Sun's magnetic field reversal, Astrophys. J. **947**, 72 (2023).

[32] E. N. Parker, The effect of adiabatic deceleration on the cosmic ray spectrum in the solar system, Planet. Space Sci. **14**, 371 (1966).

[33] U. R. Rao, Solar modulation of galactic cosmic radiation, Space Sci. Rev. **12**, 719 (1972); A. Vogt, N. Eugene Engelbrecht, B. Heber, A. Kopp, and K. Herbst, Numerical and experimental evidence for a new interpretation of residence times in space, Astron. Astrophys. **657**, A39 (2022).

[34] M. Aguilar *et al.*, Periodicities in the daily proton fluxes from 2011 to 2019 measured by the Alpha Magnetic Spectrometer on the International Space Station from 1 to 100 GV, Phys. Rev. Lett. **127**, 271102 (2021). The Φ_p data up to June 2022 including the 11-year average flux can be downloaded from the AMS website https://ams02.space/sites/default/files/publication/202402/p-table-BR.csv; https://ams02.space/sites/default/files/publication/202402/p-table-Average.csv.

[35] M. Aguilar *et al.*, Temporal structures in electron spectra and charge sign effects in galactic cosmic rays, Phys. Rev. Lett. **130**, 161001 (2023). The Φ_{e^-} data up to June 2022 including the 11-year average flux can be downloaded from the AMS website https://ams02.space/sites/default/files/publication/202402/electron-table-BR.csv; https://ams02.space/sites/default/files/publication/202402/electron-table-Average.csv.

[36] M. Aguilar *et al.*, Temporal structures in positron spectra and charge sign effects in galactic cosmic rays, Phys. Rev. Lett. **131**, 151002 (2023). The Φ_{e^+} data up to June 2022 including the 11-year average flux can be downloaded from the AMS website https://ams02.space/sites/default/files/publication/202402/positron-table-BR.csv; https://ams02.space/sites/default/files/publication/202402/positron-table-Average.csv.

[37] J. S. Perko, Solar modulation of galactic antiprotons, Astron. Astrophys. **184**, 119 (1987).

[38] S. A. Stephens and R. L. Golden, The role of antiprotons in cosmic-ray physics, Space Sci. Rev. **46**, 31 (1988).

[39] W. R. Webber and M. S. Potgieter, A new calculation of the cosmic-ray antiproton spectrum in the galaxy and heliospheric modulation effects on this spectrum using a drift plus wavy current sheet model, Astrophys. J. **344**, 779 (1989).

[40] A. W. Labrador and R. A. Mewaldt, Effects of solar modulation on the low-energy cosmic-ray antiproton/proton ratio, Astrophys. J. **480**, 371 (1997).

[41] J. W. Bieber, R. A. Burger, R. Engel, T. K. Gaisser, S. Roesler, and T. Stanev, Antiprotons at solar maximum, Phys. Rev. Lett. **83**, 674 (1999).

[42] I. V. Moskalenko, A. W. Strong, J. F. Ormes, and M. S. Potgieter, Secondary antiprotons and propagation of cosmic rays in the galaxy and heliosphere, Astrophys. J. **565**, 280 (2002).

[43] P. Bobik, M. J. Boschini, C. Consolandi, S. Della Torre, M. Gervasi, D. Grandi, K. Kudela, S. Pensotti, and P. G. Rancoita, Antiproton modulation in the Heliosphere and AMS-02 antiproton over proton ratio prediction, Astrophys. Space Sci. Trans. **7**, 245 (2011).

[44] N. E. Engelbrecht and V. D. Felice, Uncertainties implicit to the use of the force-field solutions to the Parker transport equation in analyses of observed cosmic ray antiproton intensities, Phys. Rev. D **102**, 103007 (2020).

[45] D. Bisschoff, O. P. M. Aslam, M. D. Ngobeni, V. V. Mikhailov, M. Boezio, R. Munini, and M. S. Potgieter, On the very local interstellar spectra for helium, positrons, antiprotons, deuteron, and antideuteron, Phys. At. Nucl. **84**, 1121 (2021).

[46] M. S. Potgieter, O. P. M. Aslam, D. Bisschoff, and D. Ngobeni, A perspective on the solar modulation of cosmic anti-matter, Physics **3**, 1190 (2021).

[47] O. P. M. Aslam, M. S. Potgieter, X. Luo, and M. D. Ngobeni, Modulation of Cosmic-Ray Antiprotons in the Heliosphere: Simulations for a Solar Cycle, Astrophys. J. **953**, 101 (2023).

[48] N. Fornengo, L. Maccione, and A. Vittino, Constraints on particle dark matter from cosmic-ray antiprotons, J. Cosmol. Astropart. Phys. 04 (2014) 003; M. Cirelli, D. Gaggero, G. Giesen, M. Taoso, and A Urbano, Antiproton constraints on the GeV gamma-ray excess: A comprehensive analysis, J. Cosmol. Astropart. Phys. 12 (2014) 045; C. Evoli, D. Gaggero, and D. Grasso, Secondary antiprotons as a galactic dark matter probe, J. Cosmol. Astropart. Phys. 12 (2015) 039; C.-R. Zhu, M.-Y. Cui, Z.-Q. Xia, Z.-H. Yu, X. Huang, Q. Yuan, and Y.-Z. Fan, Explaining the GeV antiproton excess, GeV γ-ray excess, and W-boson mass anomaly in an inert two Higgs doublet model, Phys. Rev. Lett. **129**, 231101 (2022).

[49] X. Sun, J. T. Hoeksema, Y. Liu, and J. Zhao, On polar magnetic field reversal and surface flux transport during Solar cycle 24, Astrophys. J. **798**, 114 (2015).

[50] A. Kounine, The Alpha Magnetic Spectrometer on the International Space Station, Int. J. Mod. Phys. E **21**, 1230005 (2012); S. Ting, The Alpha Magnetic Spectrometer on the International Space Station, Nucl. Phys. B, Proc. Suppl. **243–244**, 12 (2013); B. Bertucci, The AMS-02 detector operation in space, Proc. Sci., EPS-HEP2011 (**2011**) 67; M. Incagli, Astroparticle physics with AMS02, AIP Conf. Proc. **1223**, 43 (2010); R. Battiston, The antimatter spectrometer (AMS-02): A particle physics detector in space, Nucl. Instrum. Methods Phys. Res., Sect. A **588**, 227 (2008).

[51] See Supplemental Materials at http://link.aps.org/supplemental/10.1103/PhysRevLett.134.051002 for the AMS detector description, details of event selection, background subtraction, hysteresis analysis between $\Phi_{\bar{p}}$ and Φ_p, correlation analysis between $\Phi_{\bar{p}}$ and Φ_{e^-}, figures, and the tabulated time-dependent antiproton fluxes and 11-year time-averaged antiproton flux as functions of rigidity.

[52] K. Lübelsmeyer *et al.*, Upgrade of the Alpha Magnetic Spectrometer (AMS-02) for long term operation on the International Space Station (ISS), Nucl. Instrum. Methods Phys. Res., Sect. A **654**, 639 (2011).

[53] B. Alpat *et al.*, The internal alignment and position resolution of the AMS-02 silicon tracker determined with cosmic-ray muons, Nucl. Instrum. Methods Phys. Res., Sect. A **613**, 207 (2010).

[54] G. Ambrosi, V. Choutko, C. Delgado, A. Oliva, Q. Yan, and Y. Li, The spatial resolution of the silicon tracker of the Alpha Magnetic Spectrometer, Nucl. Instrum. Methods Phys. Res., Sect. A **869**, 29 (2017).

[55] Y. Jia, Q. Yan, V. Choutko, H. Liu, and A. Oliva, Nuclei charge measurement by the Alpha Magnetic Spectrometer silicon tracker, Nucl. Instrum. Methods Phys. Res., Sect. A **972**, 164169 (2020).

[56] F. Hauler *et al.*, The AMS-02 TRD for the International Space Station, IEEE Trans. Nucl. Sci. **51**, 1365 (2004); Ph. Doetinchem *et al.*, Performance of the AMS-02 transition radiation detector, Nucl. Instrum. Methods Phys. Res., Sect. A **558**, 526 (2006); Th. Kirn, The AMS-02 TRD on the International Space Station, Nucl. Instrum. Methods Phys. Res., Sect. A **706**, 43 (2013).

[57] V. Bindi *et al.*, Calibration and performance of the AMS-02 time of flight detector in space, Nucl. Instrum. Methods Phys. Res., Sect. A **743**, 22 (2014).

[58] M. Aguilar *et al.*, In-beam aerogel light yield characterization for the AMS RICH detector, Nucl. Instrum. Methods Phys. Res., Sect. A **614**, 237 (2010); F. Giovacchini (on behalf of AMS-RICH Collaboration), Performance in space of the AMS-02 RICH detector, Nucl. Instrum. Methods Phys. Res., Sect. A **766**, 57 (2014).

[59] C. Adloff *et al.*, The AMS-02 lead-scintillating fibres Electromagnetic Calorimeter, Nucl. Instrum. Methods Phys. Res., Sect. A **714**, 147 (2013).

[60] A. Kounine, Z. Weng, W. Xu, and C. Zhang, Precision measurement of 0.5 GeV–3 TeV electrons and positrons using the AMS electromagnetic calorimeter, Nucl. Instrum. Methods Phys. Res., Sect. A **869**, 110 (2017).

[61] J. Allison *et al.*, Recent developments in GEANT4, Nucl. Instrum. Methods Phys. Res., Sect. A **835**, 186 (2016); J. Allison *et al.*, GEANT4 developments and applications, IEEE Trans. Nucl. Sci. **53**, 270 (2006); S. Agostinelli *et al.*, GEANT4—a simulation toolkit, Nucl. Instrum. Methods Phys. Res., Sect. A **506**, 250 (2003).

[62] C. C. Finlay *et al.*, International geomagnetic reference field: The eleventh generation, Geophys. J. Int. **183**, 1216 (2010); E. Thébault *et al.*, International geomagnetic reference field: The 12th generation, Earth Planets Space **67**, 79 (2015); Geomagnetic Field Modeling Working Group, IGRF-13 model (2019), https://www.ngdc.noaa.gov/IAGA/vmod/igrf.html.

[63] P. Bobik, G. Boella, M. J. Boschini, D. Grandi, M. Gervasi, K. Kudela, S. Pensotti, and P. G. Rancoita, Magnetospheric transmission function approach to disentangle primary from secondary cosmic ray fluxes in the penumbra region,

J. Geophys. Res. **111**, A05205 (2006); N. A. Tsyganenko and M. I. Sitnov, Modeling the dynamics of the inner magnetosphere during strong geomagnetic storms, J. Geophys. Res. **110**, A03208 (2005).

[64] M. Aguilar *et al.*, Precision measurement of the proton flux in primary cosmic rays from rigidity 1 GV to 1.8 TV with the Alpha Magnetic Spectrometer on the International Space Station, Phys. Rev. Lett. **114**, 171103 (2015).

[65] Note that the data can also be downloaded in different formats from the AMS Web site https://ams02.space/sites/default/files/publication/202402/pbar-table-s1-s139.csv; https://ams02.space/sites/default/files/publication/202402/pbar-table-s140.csv; the ASI cosmic-ray database at https://tools.ssdc.asi.it/CosmicRays; and the LPSC cosmic-ray database at https://lpsc.in2p3.fr/crdb/.